

A probabilistic framework for freehand 3D ultrasound reconstruction applied to catheter ablation guidance in the left atrium

Aditya B. Koolwal · Federico Barbagli ·
Christopher R. Carlson · David H. Liang

Received: 13 January 2009 / Accepted: 26 April 2009 / Published online: 4 June 2009
© CARS 2009

Abstract

Introduction The catheter ablation procedure is a minimally invasive surgery used to treat atrial fibrillation. Difficulty visualizing the catheter inside the left atrium anatomy has led to lengthy procedure times and limited success rates. In this paper, we present a set of algorithms for reconstructing 3D ultrasound data of the left atrium in real-time, with an emphasis on automatic tissue classification for improved clarity surrounding regions of interest.

Methods Using an intracardiac echo (ICE) ultrasound catheter, we collect 2D-ICE images of a left atrium phantom from multiple configurations and iteratively compound the acquired data into a 3D-ICE volume. We introduce two new methods for compounding overlapping US data—occupancy-likelihood and response-grid compounding—which automatically classify voxels as “occupied” or “clear,” and mitigate reconstruction artifacts caused by signal dropout. Finally, we use the results of an ICE-to-CT registration algorithm to devise a response-likelihood weighting scheme, which assigns weights to US signals based on the likelihood that they correspond to tissue-reflections.

Results Our algorithms successfully reconstruct a 3D-ICE volume of the left atrium with voxels classified as “occupied” or “clear,” even within difficult-to-image regions like the pulmonary vein openings. We are robust to dropout artifact that plagues a subset of the 2D-ICE images, and our weighting scheme assists in filtering out spurious data attributed to ghost-signals from multi-path reflections. By automatically classifying tissue, our algorithm precludes the need for thresholding, a process that is difficult to automate without subjective input. Our hope is to use this result towards developing 3D ultrasound segmentation algorithms in the future.

Keywords 3D ultrasound · Occupancy grid mapping · Catheter ablation · Left atrium · Image guided surgery

Introduction

The treatment of atrial fibrillation by means of catheter ablation allows physicians to operate inside the atria without having to perform open heart surgery. Unfortunately, this procedure can be very time-consuming, as traditional imaging modalities fail to yield a clear and comprehensive picture of the surgical environment. For example, X-ray fluoroscopy images the ablation catheter with clarity, but delivers inadequate contrast for imaging cardiac tissue. Conversely, intracardiac echo (ICE) ultrasound readily images cardiac tissue, but is difficult to orient for imaging the ablation catheter tip. Further, both X-ray and ICE yield 2D images, requiring the physician to mentally piece together images taken from different views to recover 3D information.

Magnetic resonance (MR) and computed tomography (CT), on the other hand, yield high-resolution 3D images

A. B. Koolwal (✉)
Department of Mechanical Engineering, Stanford University,
Stanford, CA, USA
e-mail: koolwal@stanford.edu

F. Barbagli
Department of Computer Science, Stanford University,
Stanford, CA, USA

F. Barbagli · C. R. Carlson
Hansen Medical, Inc., Mountain View, CA, USA

D. H. Liang
Division of Cardiovascular Medicine, Stanford University,
Stanford, CA, USA

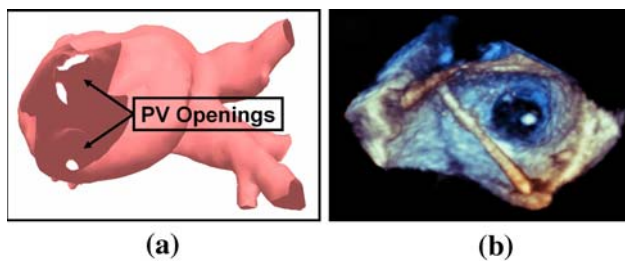


Fig. 1 3D Visualization. In **a** we see a surface mesh of the left atrium, segmented from a cardiac CT scan. The mesh provides a gross anatomic view of the entire left atrium, while still retaining high-resolution detail of smaller features such as the pulmonary vein (PV) openings (*white circles*). In **b** we see a 3D ultrasound image taken of a PV opening (*dark circle*) and ablation catheter (*line pointed down*). While 3D ultrasound is updated in real-time, it can only image a small volume of space

from which tissue surface meshes can be segmented, facilitating visualization (Fig. 1a). A 3D surface mesh of the atrium would be ideal for catheter ablation guidance, but traditional MR and CT imaging systems can only be used in a pre-operative setting. Real-time CT can be approximated intra-operatively using rotational X-ray angiography [1,2], but the patient is administered a large dose of radiation for each generated volume [3].

3D ultrasound (3D-US) has gained popularity because it is relatively cheap and harmless to the patient. Unfortunately, the trans-esophageal echo (TEE) probe—which is best-suited for intra-operative acquisition of cardiac 3D-US—has a fairly limited field-of-view (Fig. 1b). Further, cardiac 3D-US is generally difficult to segment for surface mesh reconstruction and catheter tip identification [4–7]. Because of its size, the TEE probe requires patient-intubation, a risk physicians prefer not to take unless explicitly required. Recent advancements in transducer miniaturization have enabled the development of a 3D-ICE transducer that fits in a 7 Fr catheter, allowing for real-time 3D-US imaging from within the heart [8]. However, 3D-ICE currently suffers from the same limitations with respect to field-of-view; this may persist even as the 3D-ICE probe undergoes further development simply because a smaller probe precludes imaging a large volume.

Extended-field-of-view of ultrasound (EFOV-US), where several 2D-US images are acquired from different probe orientations and merged into the same volume, can be employed to approximate 3D-US [9]. In the cardiac setting, a collection of 2D-ICE images can be acquired by rotating the ICE catheter axially (Fig. 2) to sweep out a 3D-ICE volume [10]. While there is copious literature on EFOV-US [9,11], automatic segmentation of cardiac ultrasound remains an open issue. As a result, cardiac 3D-US and EFOV-US is typically volume-rendered for visual presentation [12,13], but structures are not as clearly identifiable as they are in a properly segmented surface mesh.

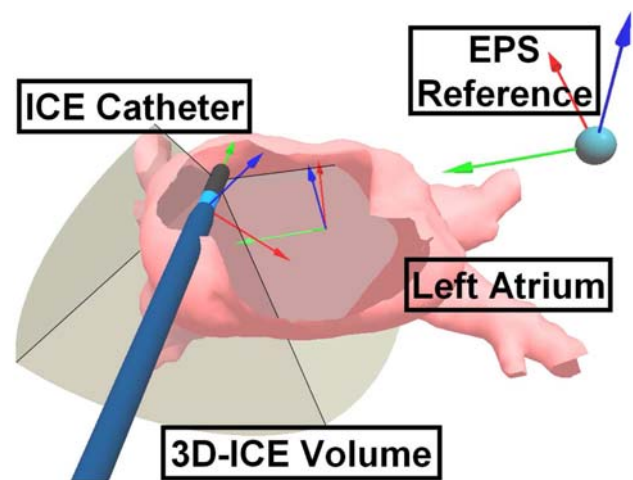


Fig. 2 3D-ICE Acquisition. The ICE catheter is rotated axially to image a swept volume of the left atrium. An electromagnetic position sensor (EPS) is used to track the ICE catheter's tip to ensure proper insertion of 2D-ICE slices into the reconstructed volume. In the above example, the ICE catheter is well-situated for imaging the posterior wall of the left atrium, but not the pulmonary veins

Contributions

In this paper we present a method for real-time reconstruction of 3D-US volumetric data that incrementally classifies voxels as representing tissue or free-space. Our approach is motivated by a desire to reconstruct data that approach the level of clarity of a segmented surface mesh, in a completely automated fashion.

We stitch together 2D-ICE images obtained from an ICE catheter that moves freely within a left atrium phantom model, reconstructing a 3D-ICE volume. The “freehand” imaging technique enables data acquisition from multiple vantages at multiple resolutions, allowing us to gradually add missing details to the 3D-ICE volume as needed.

Rather than employing weighted-average compounding—the standard algorithm for managing overlapping data—we use an occupancy-likelihood technique taken from occupancy grid mapping [14,15]. Occupancy grids are probabilistic maps used to predict which regions of space are “occupied” and which regions are “clear.” As we continuously acquire 2D-ICE data in a particular region of space, we incrementally classify whether we believe tissues are present or not in the region. Not only does this classification facilitate volume visualization, it can be useful downstream for tissue segmentation—an active area of research in 3D-US.

If the ICE probe is oriented poorly when collecting data around a specific region of tissue, the acquired images will suffer from dropout, and we might infer that tissues do not exist in the region. However, if we re-collect data around the same region from a better orientation, the acquired images

will indicate tissue presence. Occupancy-likelihood compounding on its own will treat data from both acquisitions equally, resulting in classification uncertainty. To resolve this issue, we split 2D-ICE contributions into different “response groups,” where each response group manages data from ultrasound pulses within a restricted set of incidence angles. This way, if ultrasound response signals are weak from a certain direction, they will not negatively impact our classification algorithm if response signals are strong from another direction.

Finally, we incorporate previous work where we devised a method for registering ICE ultrasound to a CT-derived surface mesh of the anatomy, acquired in a pre-operative setting [16]. Using the results of this registration, we can estimate which ultrasound signals correspond to tissue reflections, and which might be caused by ghost-reflections. This technique allows us to clip out data that do not correspond to the anatomy, further improving our tissue classification algorithm.

Related work

In the catheter ablation procedure, ablation lines are “drawn” over tissue surfaces in the left atrium. Of particular interest are the posterior wall, the pulmonary vein (PV) openings, and the atrium’s roof [17]. While the longitudinal distance across the atrium can be as large as ≈ 80 mm, the PV openings on either side are on the order of ≈ 10 mm in diameter [18]. As such, not only is it important to visualize the entire atrium for aiding gross catheter movements, it is also important to have a high-resolution exploded view of the PVs to aid in precise tracing of circular ablation lines around the PV openings.

The lack of adequate imaging techniques for catheter guidance has led to a variety of sensor-based visualization techniques. Perhaps the most widely adopted involves the use of electromagnetic position/orientation sensors (EPS) that record the location of the catheter’s tip in space. Of particular interest is the commercially available CartoSound[®] system (Bio-Sense Webster, Diamond Bar, CA, USA), which tracks both the ablation catheter and an ICE catheter using EPS sensors. The ICE catheter is rotated axially while acquiring several images of the left atrium, and the images are manually segmented to identify tissue surface contours. Once manual segmentation is complete, a 3D mesh is built over these contours to roughly approximate the shape of the atrium. Finally, the sensorized ablation catheter is displayed within this mesh to facilitate guidance.

A deficiency of this approach is that the resulting mesh does not always accurately capture tissue surface boundaries over the entire atrium because it is highly interpolated over a sparse sampling of contours. While accurate in the

regions where ICE images have already been acquired and segmented, the best way to guarantee accuracy in regions that have yet to be imaged is to acquire and segment additional images. Consequently, the amount of time required to generate an accurate map can be lengthy, on the order of 20–30 min according to recent studies [19,20].

A faster, automated approach for generating a tissue surface map of the left atrium would be preferable, and 3D-US imaging is a viable alternative to surface mesh reconstruction approaches. Clinically, 3D-US is a valuable tool for surgical guidance because physicians are already trained to read 2D-US, and it allows them to collectively visualize several anatomic features without having to mentally piece together separate 2D slices [9].

A number of techniques have been proposed for reconstructing 3D-US from 2D-US data, including fixed-geometry and freehand approaches. In fixed-geometry reconstruction, a mechanical system moves the US probe along a fixed trajectory, sweeping out a volume whose structure is known *a priori*. Freehand reconstruction, on the other hand, is more flexible, allowing 2D-US contributions from arbitrary probe positions and orientations. Frequently, a sensor similar to the EPS described above is mounted to the probe so the transformation mapping image pixels to volume voxels can be computed in real-time [21]. A number of ultrasound manufacturers have developed electronics and software to enable this technique, including Siescape[®] (Siemens Ultrasound, Issaquah, WA, USA) and LOGIQView[®] (GE Medical Systems, Waukesha, WI, USA) [22].

One advantage of using freehand instead of fixed-geometry reconstruction is that it provides a better demonstration of the spatial relationships among structures when the size of a single volume is not large enough to cover the structures [23]. For example, during the catheter ablation procedure, the ICE catheter is typically positioned in the right atrium when imaging the left atrium [10]. While this configuration is sufficient for imaging the left atrium’s posterior wall (Fig. 2), it is not as well-suited for imaging the PVs, which can be better captured through imaging from within the left atrium [20]. When using freehand reconstruction, the ICE catheter can be steered into the left atrium and reoriented to get a better view of the PV openings. Furthermore, freehand reconstruction allows for spatial compounding, whereby tissues are imaged from multiple vantages, and spurious signals related to ghost reflections and motion artifact are averaged out. This can significantly improve signal to noise ratio in the reconstructed volume [9].

By incorporating data acquired from a number of different vantage points, the resulting volume can potentially capture a high level of detail for all structures of interest; this is of great clinical value to the catheter ablation procedure, where ablation therapy is delivered throughout the left atrium in its entirety.

Methods

Ultrasound phantom and ICE acquisition

We evaluate the performance of our 3D-ICE reconstruction algorithms in vitro using an ultrasound phantom in the shape of a left atrium. To create the phantom we segmented a cardiac CT scan using Verizmo (*St. Jude Medical, Minneapolis, MN*), generating a surface mesh of the left atrium and PVs. The surface mesh was used to fabricate a 3D stereo lithography (SLA) model, whose impression was cast in 0.1% silicone dioxide. The resultant cavity-mold was bead-blasted to generate a textured surface, exhibiting tissue-like reflectivity when imaged under ultrasound.

The ultrasound phantom is submerged in a water bath and an AcuNav ICE catheter (*Siemens Ultrasound, Mountain View, CA*) is manually positioned inside the phantom for imaging (Fig. 3). The ICE catheter is attached to a Sequoia Ultrasound System (*Siemens Ultrasound, Mountain View, CA*), whose output images are frame-grabbed onto a PC using a Foresight I-Color frame-grabber (*Foresight, Boston, MA*) at a rate of 15 Hz. Frame-grabbed images are resampled into a series of 128 scan-lines (SL_i) that are equally-spaced angularly, with 128 samples ($SL_{i,j}$) on each line. This representation simplifies computations required for response-grid compounding (described in Section “Response-Grid Compounding”).

We chose a 128×128 sampling based on the maximum ICE acquisition depth (50 mm) and the volume voxel spacing ($[1 \text{ mm} \times 1 \text{ mm} \times 1 \text{ mm}]$, described in Section “Freehand 3D-ICE Reconstruction”). To prevent gaps from being introduced into the reconstructed volume upon insertion of a new ICE image, we must ensure that adjacent scan-line samples are less than 1 mm apart. For a 90° sector ICE image acquired at 50 mm depth, we require

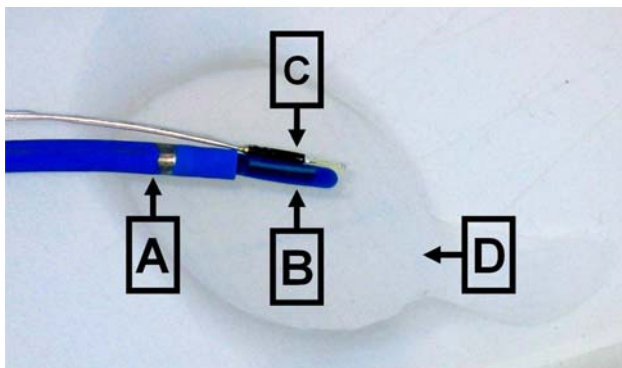


Fig. 3 ICE acquisition of ultrasound phantom. The ICE catheter is run up through a sheath A for stability, and its tip emerges from the sheath's lumen B. A sensor C is mounted to the ICE catheter's tip for monitoring movement. The ICE catheter images a left atrium phantom D serving as an anatomical proxy

$$\# \text{ samples} \geq \frac{50 \text{ mm}}{1 \text{ mm}} = 50 \quad (1)$$

and

$$\# \text{ scanlines} \geq \frac{50 \text{ mm} \cdot \frac{\pi}{2} \text{ rad}}{1 \text{ mm}} = 78.5 \quad (2)$$

Therefore, 128 scan-lines with 128 samples is sufficient to ensure no gaps are introduced.

A 6-DOF position/orientation sensor (*Ascension Technologies, Burlington, VT*) is affixed to the ICE catheter tip to monitor its movement. We determined the transformation relating ICE pixels to sensor coordinates using a single-target calibration phantom described in [24].

Freehand 3D-ICE reconstruction

We approximate that the left atrium, at its largest, will occupy a volume of $100 \text{ mm} \times 100 \text{ mm} \times 100 \text{ mm}$. For this reason we choose the dimensions of 3D-ICE volume V to be $V^D = [200 \text{ mm} \times 200 \text{ mm} \times 200 \text{ mm}]^T$; this way, if we initialize the ICE catheter to be at the center of the volume, we can ensure the entire imaged atrium will fall inside the volume, regardless of how the ICE catheter is initially positioned with respect to the atrium. We chose the voxel spacing in accordance with the expected amount of out-of-plane ultrasound beam spreading, which is typically on the order of $\approx 2.5^\circ$ [25]. When acquiring ICE images at 50 mm depth, the average amount of beam spreading for a given scan-line sample is $\approx 1.45 \text{ mm}$. As such, our voxel spacing is set to $V^S = [1 \text{ mm} \times 1 \text{ mm} \times 1 \text{ mm}]^T$. We are careful to acquire a dense sampling of 2D-ICE images to ensure that no holes or gaps appear in V between consecutively inserted images.

We insert scan-line sample values $SL_{i,j}^v$ into V using voxel nearest neighbor (VNN) interpolation with spatial compounding. Each voxel ($v_n \in V$) maintains a cumulative weight and value counter (v_n^w and v_n^v). At time $t = k$, when $SL_{i,j}^v$ is compounded into v_n , the counters are incremented as follows:

$$v_{n_k}^w = v_{n_{k-1}}^w + 1 \quad (3)$$

$$v_{n_k}^v = f_{\text{cmp}}(SL_{i,j}^v, v_{n_{k-1}}^v, v_{n_{k-1}}^w) \quad (4)$$

where f_{cmp} is the spatial compounding function used to accumulate multiple $SL_{i,j}^v$ contributions. Throughout the remainder of this paper, we assume the $SL_{i,j}^v$ are normalized to take on values ranging from 0 to 1:

$$0 \leq SL_{i,j}^v \leq 1 \quad (5)$$

and that

$$0 \leq v_n^v \leq 1 \quad (6)$$

The specific definition of f_{cmp} depends on the type of compounding performed; in this paper, we employ three

strategies—weighted-average, occupancy-likelihood, and response-grid compounding, the last of which is used in combination with either of the first two. Weighted-average compounding is frequently used in the 3D-US literature [11, 26] as a standard approach to spatial compounding. Occupancy-likelihood and response-grid compounding are variants of algorithms used for mapping in mobile robotics. To the best of our knowledge, these two techniques have yet to be employed in medical ultrasound reconstruction.

Weighted-average compounding

Weighted-average compounding (WAC) is frequently used in freehand 3D-US reconstruction because its simplicity allows for real-time volume-updating. The WAC compounding function is defined as

$$f_{\text{cmp}}^{\text{wac}} \left(\text{SL}_{i,j}^v, v_{n_{k-1}}^v, v_{n_{k-1}}^w \right) = \frac{v_{n_{k-1}}^w v_{n_{k-1}}^v + \text{SL}_{i,j}^v}{\left(v_{n_{k-1}}^w + 1 \right)} \quad (7)$$

WAC is useful for removing specular artifact from ultrasound data, yielding smooth and continuous surfaces in its 3D-US reconstructions. However, it is not well-suited for classification since an additional thresholding step must be employed to classify tissues, which is difficult to automate.

Occupancy-likelihood compounding

To automatically classify voxel occupancy without subjective input, we employ occupancy-likelihood compounding (OLC). OLC is based on occupancy grid mapping (OGM), a strategy used in robotics to find obstacles in an unknown environment.

In an occupancy grid map, the environment is represented by a grid of voxels, where each voxel is either occupied by an obstacle or not. This framework applies directly to the medical ultrasound setting, where the presence of signal content in a US image corresponds to tissue boundaries that occupy space. We represent the occupancy state of voxel v_n with a binary random variable \mathbf{v}_n , where \mathbf{v}_n can take on one of two values: “occupied” or “clear.” For brevity, we refer to the probability that v_n is occupied as $p(\mathbf{v}_n = \text{occupied}) = p(\mathbf{v}_n)$.

The likelihood that v_n is occupied can be determined by considering all the ultrasound scans-line samples compounded into v_n . At time $t = k$, contributing sample $\text{SL}_{i,j}$ is referred to as *measurement* \mathbf{z}_k . Given the history of all measurements $\mathbf{z}_1 \dots \mathbf{z}_k = \mathbf{z}_{1:k}$, the likelihood that v_n is occupied is simply $p(\mathbf{v}_n | \mathbf{z}_{1:k})$. In other words,

$$v_{n_k}^v = p(\mathbf{v}_n | \mathbf{z}_{1:k}) \quad (8)$$

Therefore, the OLC compounding function is defined as:

$$f_{\text{cmp}}^{\text{ole}} \left(\text{SL}_{i,j}^v, v_{n_{k-1}}^v, v_{n_{k-1}}^w \right) = p(\mathbf{v}_n | \mathbf{z}_{1:k}) \quad (9)$$

As described in [15], $p(\mathbf{v}_n | \mathbf{z}_{1:k})$ can be computed using an odds-representation:

$$\text{odds}(\mathbf{v}_n)_k = \frac{p(\mathbf{v}_n | \mathbf{z}_{1:k})}{p(\neg \mathbf{v}_n | \mathbf{z}_{1:k})} \quad (10)$$

with recursive formulation

$$\text{odds}(\mathbf{v}_n)_k = \left(\frac{p(\mathbf{v}_n | \mathbf{z}_k)}{p(\neg \mathbf{v}_n | \mathbf{z}_k)} \frac{p(\neg \mathbf{v}_n)}{p(\mathbf{v}_n)} \right) \text{odds}(\mathbf{v}_n)_{k-1} \quad (11)$$

Negated probabilities $p(\neg \mathbf{v}_n)$ are simply computed as

$$p(\neg \mathbf{v}_n) = 1 - p(\mathbf{v}_n) \quad (12)$$

Finally, occupancy likelihood $p(\mathbf{v}_n | \mathbf{z}_{1:k})$ can be recovered from Eqs. 10 and 12 through algebraic manipulation:

$$\begin{aligned} p(\mathbf{v}_n | \mathbf{z}_{1:k}) &= p(\neg \mathbf{v}_n | \mathbf{z}_{1:k}) \text{odds}(\mathbf{v}_n)_k \\ &= (1 - p(\mathbf{v}_n | \mathbf{z}_{1:k})) \text{odds}(\mathbf{v}_n)_k \\ &= \frac{\text{odds}(\mathbf{v}_n)_k}{(1 + \text{odds}(\mathbf{v}_n)_k)} \end{aligned} \quad (13)$$

Combining Eqs. 9 and 13, we can compute $f_{\text{cmp}}^{\text{ole}}$ as:

$$f_{\text{cmp}}^{\text{ole}} \left(\text{SL}_{i,j}^v, v_{n_{k-1}}^v, v_{n_{k-1}}^w \right) = \frac{\text{odds}(\mathbf{v}_n)_k}{(1 + \text{odds}(\mathbf{v}_n)_k)} \quad (14)$$

Probabilities $p(\mathbf{v}_n)$ and $p(\mathbf{v}_n | \mathbf{z}_k)$ in Eq. 11 are determined using application-specific models of likelihood. We chose the prior probability of voxel occupancy to be

$$p(\mathbf{v}_n) = 0.1 \quad (15)$$

This number was determined by taking a CT-based surface mesh of the anatomy and computing the percentage of voxels representing tissue in the volume subsuming the mesh. To compute sensor model $p(\mathbf{v}_n | \mathbf{z}_k)$, we assume that all signal content in the 2D-ICE images is valid, since medical ultrasound can detect multiple obstacle boundaries along the path of a single scan-line. The simplest solution is to equate the conditional likelihood of occupancy to the normalized scan-line sample value $\text{SL}_{i,j}^v$:

$$p(\mathbf{v}_n | \mathbf{z}_k) = \text{SL}_{i,j}^v \quad (16)$$

where

$$0 \leq p(\mathbf{v}_n | \mathbf{z}_k) \leq 1 \quad (17)$$

In order for this sensor model to work properly, we reduce the dynamic range and increase the gain on the ultrasound scanner to ensure imaged tissue will yield high-likelihood measurements. By reducing the dynamic range we are essentially throwing away information, but the notion of classifying voxels as either “occupied” or “clear” inherently requires this loss of information.

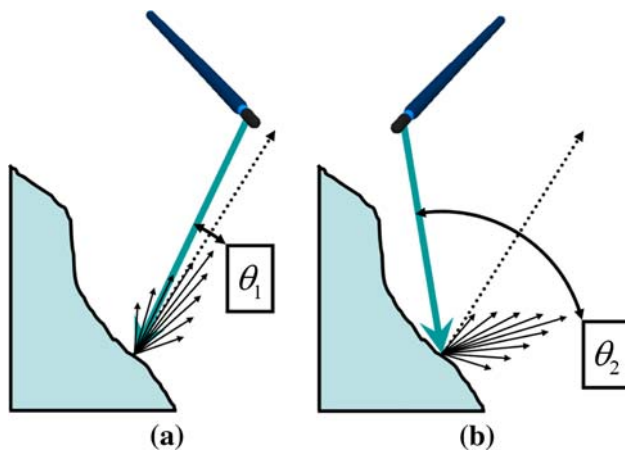


Fig. 4 Received reflection strength. Contingent on the angle of incidence between an ultrasound scan-line and the tissue surface it encounters, reflections of varying magnitudes will be sent back to the transducer. Because of scattering due to imperfections on the tissue's surface, the scan-line incidence angle need not be exactly normal to the surface (a) in order to generate a strong reflection that returns back to the transducer. However, should the disparity between incidence angle and surface normal grow too large (b), a very weak reflection—or no reflection at all—is sent back

Finally, we fold Eqs. 8, 10, 15, and 16 into Eq. 11 to compute odds $(v_n)_k$:

$$\text{odds } (v_n)_k = 9 \frac{SL_{i,j}^v}{(1 - SL_{i,j}^v)} \frac{v_{n_{k-1}}^v}{(1 - v_{n_{k-1}}^v)} \quad (18)$$

which is used in Eq. 14 to compute $f_{\text{cmp}}^{\text{olc}}(SL_{i,j}^v, v_{n_{k-1}}^v, v_{n_{k-1}}^w)$.

Response-grid compounding

While OLC is useful for classifying the presence of tissue or lack thereof in a volume, it is not well-suited for dealing with ultrasound signal dropout. Dropout occurs when imaging tissue from a vantage that does not return strong reflections back to the transducer. If we assume that the strength of the reflection returning to the transducer is proportional to angle between the scan-line incidence angle and the tissue surface normal (Fig. 4), when the angle grows too large we may not receive a reflection at all (Fig. 4b). In this situation we might infer that tissue is not present, even though it is. Furthermore, if we continuously image from poorly chosen vantage points, both WAC and OLC compounding algorithms will compute results indicating a lack of tissue, even if some of the recorded data suggests otherwise.

To deal with this dilemma, we use the response-grid compounding (RGC) algorithm described in [27] for sonar mapping in highly specular environments. The idea behind response-grid compounding is simple. For each voxel v_n , we assign an $SL_{i,j}$ contribution to one of M different “response-

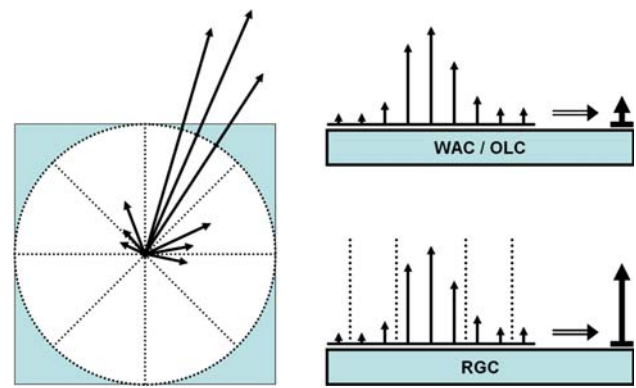


Fig. 5 Response-grid compounding. In this 2D example, ultrasound scan-lines intersecting a pixel are assigned to one of 8 different “response groups” depending upon their angle of incidence with the pixel (left). Reflections sent back in response to scan-line impulses are denoted by arrows whose lengths correlate to reflection strength. We see that some scan-lines generate strong reflections, while others generate considerably weaker reflections. On their own, WAC and OLC compounding (top right) will average all reflections together, yielding a weak overall response. RGC (bottom right), on the other hand, only averages reflections within response groups. As long as one group average indicates a strong response, the overall response will be strong as well

groups” (G_m) based on the scan-line's entry-angle into v_n . Each G_m has its own value and weight counters— G_m^v and G_m^w —incremented according to Eqs. 3 and 4 (with G_m replacing v_n). Finally, each G_m has an occupancy state represented by binary random variable g_m , with a conditional likelihood of occupancy equivalent to $p(g_m | \mathbf{z}_{1:k})$. We now compute $p(v_n | \mathbf{z}_{1:k})$ as

$$\begin{aligned} p(v_n | \mathbf{z}_{1:k}) &= p(g_1 | \mathbf{z}_{1:k}) \vee p(g_2 | \mathbf{z}_{1:k}) \\ &\quad \times \vee \dots \vee p(g_{M-1} | \mathbf{z}_{1:k}) \vee p(g_M | \mathbf{z}_{1:k}) \\ &= 1 - \prod_{m=1}^M (1 - p(g_m | \mathbf{z}_{1:k})) \end{aligned} \quad (19)$$

The RGC compounding function is thus defined as

$$\begin{aligned} f_{\text{cmp}}^{\text{rhc}}(SL_{i,j}^v, v_{n_{k-1}}^v, v_{n_{k-1}}^w) \\ = 1 - \prod_{m=1}^M \left(1 - f_{\text{cmp}}^{\text{xxx}}(SL_{i,j}^v, G_{m_{k-1}}^v, G_{m_{k-1}}^w) \right) \end{aligned} \quad (20)$$

where $SL_{i,j}$ is only inserted into one of the G_m , and $f_{\text{cmp}}^{\text{xxx}}$ can be either $f_{\text{cmp}}^{\text{wac}}$ or $f_{\text{cmp}}^{\text{olc}}$. In Fig. 5 we see a 2D example demonstrating the advantage of RGC over WAC and OLC.

Figure 6 illustrates how we assign $SL_{i,j}$ contributions to different response groups. We represent v_n as a virtual sphere penetrated by scan-lines at different points on its surface.

Using a two-angle, pitch-yaw (β, γ) parametrization, we split v_n 's surface into M regions, where each region represents a different response group (Fig. 6a). Based on the incidence angle of scan-line SL_i as it travels outwards from the

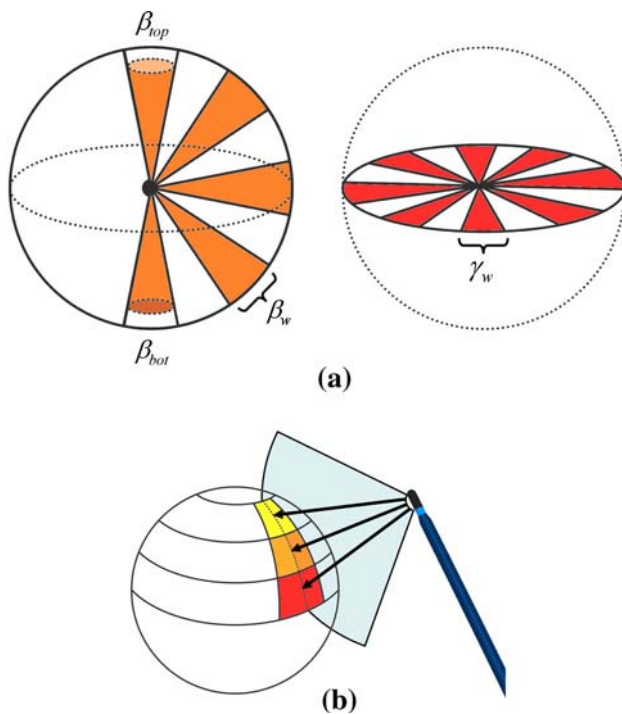


Fig. 6 Response group assignment. In **a** we parametrize the voxel's surface using pitch (β) and yaw (γ) angles, then split the pitch-angle range into 9 windows (β_w) and the yaw-angle range into 16 windows (γ_w). A response group is assigned to each (β_w, γ_w) combination with the exception of β_{bot} and β_{top} , who are each assigned one group for all γ_w . In **b** we determine which response group an ultrasound scan-line sample is compounded into on the basis of its entry angle into the voxel

ICE transducer, we can quickly compute which G_m to assign its samples to (Fig. 6b).

Our group-splitting algorithm is described at the bottom of Fig. 6. In total there are $M = 114$ response groups. As M grows large, RGC is better able to combat ultrasound dropout. However, the space required to manage the response grid data structure increases linearly with M , so finding an optimal trade off between memory allocation and resolution is necessary.

Response-likelihood weighting

In Section “Occupancy-Likelihood Compounding” we made the assumption that 2D-ICE images contain no spurious reflections. However, this is generally not true; our acquired ICE images suffer from ghost signal artifact, typically caused by multi-path reflections. To suppress contributions from ghost artifacts, we employ a response-likelihood weighting (RLW) scheme based on an initial registration of 3D-ICE volume V to the left atrium surface mesh.

In [16] we described a stochastic method for automatically localizing an ICE catheter inside the left atrium given an anatomically-representative surface mesh.

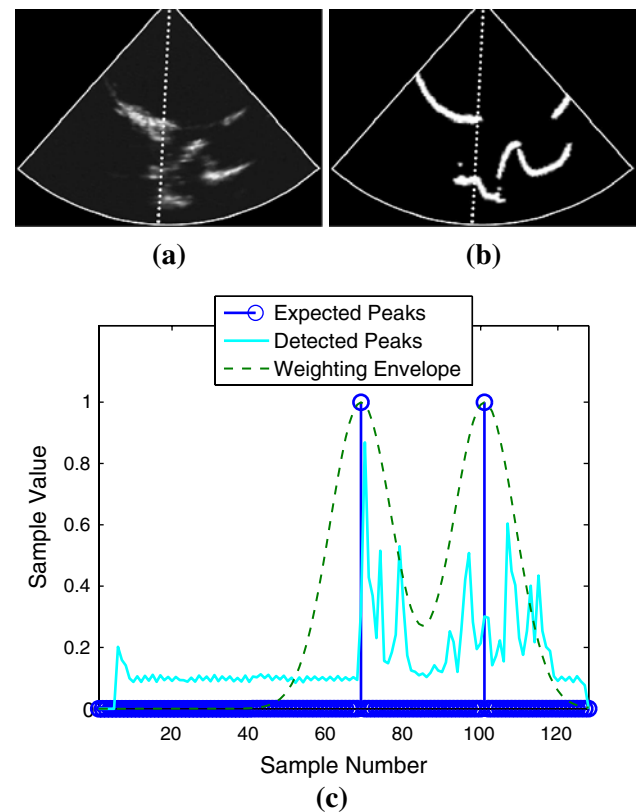


Fig. 7 Response-likelihood weighting. To distinguish valid reflections from ghost reflections, we compare scan-line data from a real ICE image **a** and its virtual ICE image counterpart **b**. In **c** we use the virtual scan-line data to determine peak locations where valid reflections are likely to occur. We convolve a Gaussian curve over these peaks to generate scan-line sample weights $SL_{i,j}^w$. Samples close to—but not co-located with—expected peak positions are assigned non-zero weights because the true shape of the anatomy may differ from that of the mesh used to generate virtual scan-line data. Scan-line sample values $SL_{i,j}^v$ are multiplied by their corresponding weight prior to compounding

We also described an algorithm for generating “virtual ICE images” of the left atrium surface mesh based on a simplified model of ultrasound reflections (Fig. 7b). These virtual images can be re-sampled into a series of virtual scan-lines (VL_i) whose samples ($VL_{i,j}$) share a one-to-one correspondence with the $SL_{i,j}$.

As illustrated in Fig. 7, we can predict which of the $SL_{i,j}^v$ represent valid reflections based on virtual scan-line values $VL_{i,j}^v$, and compute weights ($SL_{i,j}^w$) for each $SL_{i,j}$ accordingly. Figures 7a and b show the real and virtual ICE images from a particular acquisition along with an overlaid scan-line. Figure 7c shows real scan-line sample data plotted against peaks at indices where we expect to see reflections, computed on the basis of virtual scan-line data. We convolve the expected-peak signal with a Gaussian kernel ($\mathcal{N}(0, \sigma_w)$) yielding a weighting envelope that defines $SL_{i,j}^w$ for each scan-line sample, where $0 \leq SL_{i,j}^w \leq 1$. Then, rather than

using $SL_{i,j}^v$ as an input to f_{cmp} , we use the product $SL_{i,j}^w \cdot SL_{i,j}^v$ instead.

Gaussian kernel parameter σ_w allows us to account for slight differences between the left atrium surface mesh and the anatomy. Frequently, the shape of the anatomy changes after the patient undergoes a pre-operative CT/MR study, and because the surface mesh is derived from this study, it may be “out-of-date” when the procedure begins. Even if the surface mesh does not match the anatomy’s morphology, we still retain contributions from scan-line samples that are close to the expected-peak locations. We chose σ_w to be 3.33 mm, allowing data within 10 mm of the expected surface boundary to be incorporated into V . This parameter can be increased or decreased in accordance to how “out-of-date” our surface mesh is.

Results

3D-ICE volume accuracy

To evaluate the accuracy of our 3D-ICE reconstruction algorithms, we use a modified version of the occupancy grid *match* algorithm, first described in [28]. Briefly, *match* measures the similarity between occupancy grid maps V_1 and V_2 by going through each pair of overlapping voxels ($v_{n1} \in V_1$ and $v_{n2} \in V_2$) and computing the probability that v_{n1} and v_{n2} represent the same information. Because the vast majority of our reconstructed 3D-ICE volume is empty space, we modify the *match* algorithm to only include overlapping voxel pairs when either v_{n1}^v or v_{n2}^v is non-zero. Finally, we normalize our results so that $0 \leq \text{match}(V_1, V_2) \leq 1$, where $\text{match}(V_1, V_2) = 1$ indicates a perfect match.

For each 3D-ICE volume, we first classify voxels as “occupied” or “clear” by thresholding at cutoff value c , then compute the *match* score of the thresholded volume. We repeat this process over the entire range of plausible threshold values ($0 < c < 1$).

In the following sections, we evaluate the performance of our 3D-ICE reconstruction algorithms using a “gold-standard” voxel map based on the left atrium surface mesh. The gold-standard is reconstructed from planar cross-sections of the surface mesh, taken from the same set of ICE catheter poses measured during acquisition; each cross-section corresponds to an acquired ICE image, with the same pixel dimensions and spacing.

Compounding regions of interest

In the catheter ablation procedure, ablation lines are “drawn” over tissue surfaces in the left atrium. Of particular interest are the posterior wall, the PV openings, and the atrium’s roof [17]. ICE catheters are typically placed in the right atrium, a

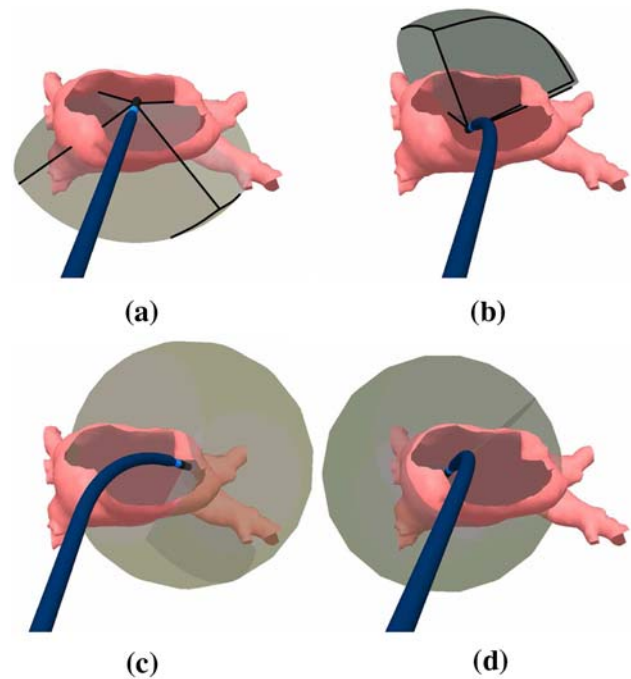


Fig. 8 Compounding regions of interest. To properly reconstruct a 3D-ICE volume of the left atrium, we image different regions of interest from different vantages. In the above illustrations we see the catheter configurations used to image each region, as well as the volume swept out by rotating the catheter axially while imaging. In **a** we image the posterior wall. In **b** we image the roof of the atrium. In **c** and **d** we image the left and right PV openings, respectively

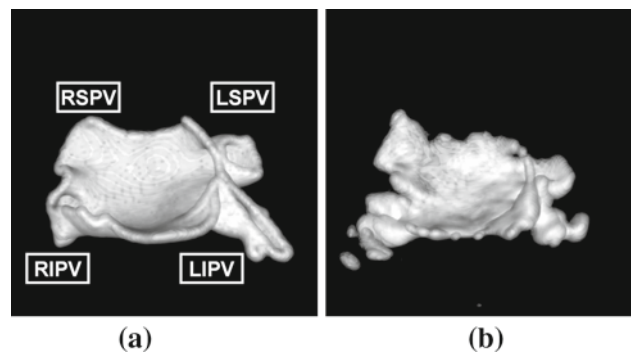


Fig. 9 Posterior wall imaging. Using the configuration shown in Fig. 8a, we image a swept volume of the atrium’s posterior wall. In **a** we see the gold-standard voxel map of the imaged-volume with the left inferior, left superior, right inferior, and right superior PVs shown (LIPV, LSPV, RIPV, RSPV, respectively). In **b** we see the corresponding 3D-ICE volume reconstructed using WAC. PV openings are clearly visible in the gold-standard map, but do not appear in the 3D-ICE volume because of dropout

configuration ideal for imaging the posterior wall (Fig. 8a). However, we see that a 3D-ICE volume generated by rotating an ICE catheter axially from this configuration fails to image the PV openings and the roof in their entirety (Fig. 9).

To obtain a more complete representation of the atrium, we image from a multitude of configurations and compound

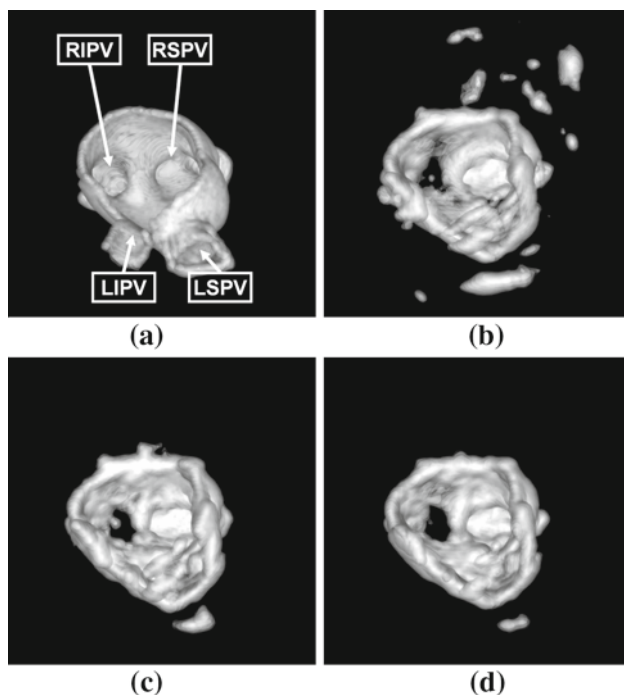


Fig. 10 Right pulmonary vein imaging. We reconstruct 3D-ICE volumes using ICE images acquired from the catheter configuration shown in Fig. 8b. The volume in **a** is the gold-standard voxel map with the left inferior, left superior, right inferior, and right superior PVs shown (LIPV, LSPV, RIPV, RSPV, respectively). The volume in **b** is reconstructed using WAC compounding alone. The volume in **c** is reconstructed using WAC with RGC and RLW, and the volume in **d** is reconstructed using OLC with RGC and RLW. Because of ultrasound dropout, we cannot see the left PVs in our 3D-ICE volumes (**b**, **c**, and **d**)

all acquired data into the same volume. In the context of the catheter ablation procedure, this would require steering the ICE catheter across the septum into the left atrium for imaging. After imaging the posterior wall, we image the left and right PV openings (Figs. 8c, d), adding detail to the volume shown in Fig. 9b. Finally, we image the atrium's roof from two configurations (Fig. 12a) to highlight the need for employing RGC or some similar scheme that accommodates dropout data.

Pulmonary vein imaging

Here we present results from imaging the right inferior and superior PV openings using the catheter configuration shown in Fig. 8d. In Fig. 10 we see a series of 3D-ICE volumes reconstructed using different compounding algorithms, compared against a gold-standard voxel map (Fig. 10a). In particular, we see volumes reconstructed using WAC only (Fig. 10b), WAC with RGC and RLW (Fig. 10c), and OLC with RGC and RLW (Fig. 10d). It is visually apparent that the addition of RGC and RLW lead to more accurate reconstructions. These perceived results are quantitatively corroborated

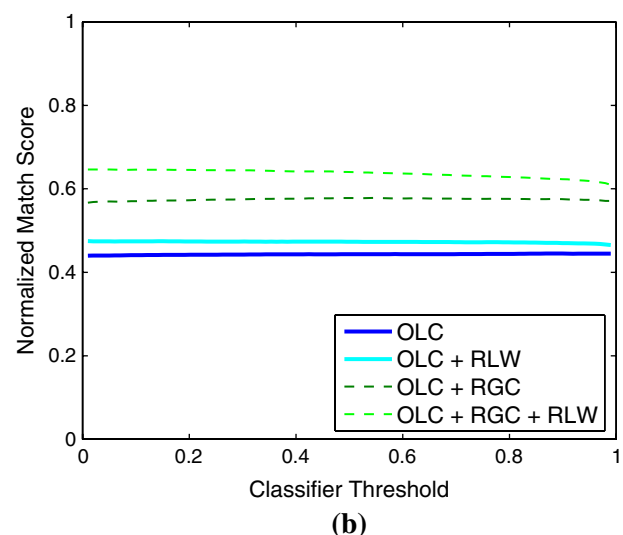
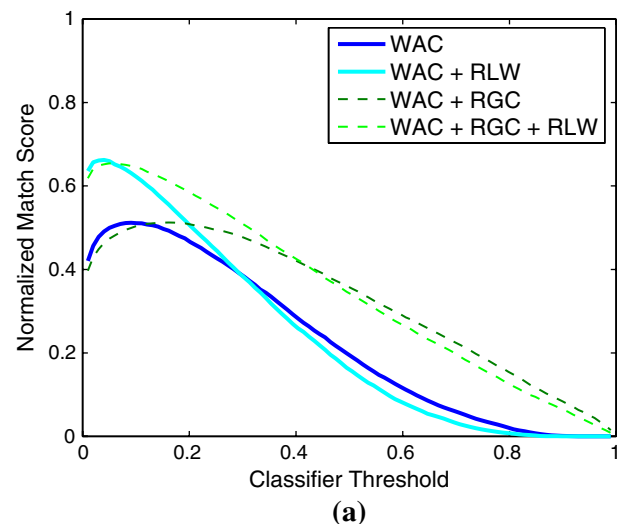


Fig. 11 Right pulmonary vein imaging match scores. To measure reconstruction accuracy, we threshold 3D-ICE volumes using cutoff value c and compute the thresholded volume's normalized *match* score. The gold-standard voxel map is used as the comparator. We repeat this process for threshold values ranging from 0 to 1. In **a** we see *match* scores for volumes reconstructed using WAC and in **b** we see *match* scores for volumes reconstructed using OLC

by evaluating the *match* scores of the different reconstructions.

In Fig. 11 we split our results into two groups: WAC-compounded volumes (Fig. 11a) and OLC-compounded volumes (Fig. 11b). Within each group, we evaluate results for the base compounding algorithm (WAC or OLC), base compounding with RLW, RGC-compounding, and RGC-compounding with RLW.

As expected, the major difference between WAC and OLC volumes is that WAC's accuracy depends entirely on the threshold cutoff used for voxel classification. Because classification is inherent to the OLC algorithm, OLC's accuracy is only marginally effected by the threshold cutoff value.

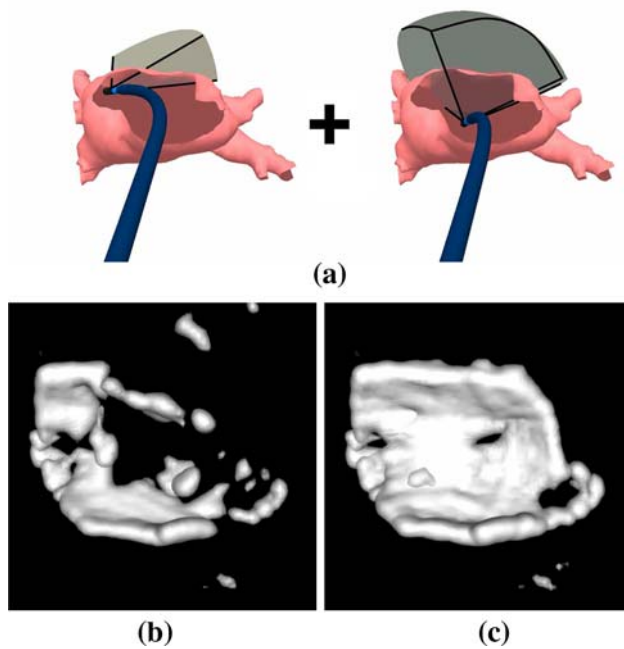


Fig. 12 Left atrium roof imaging. We image the left atrium roof using a combination of the two configurations shown in **a**. The first configuration yields poor ultrasound reflections that suffer from dropout, while the second configuration yields much stronger reflections. When using WAC compounding alone **b**, a portion of the roof is missing from the resulting 3D-ICE volume because the dropout data negates contributions from reflections indicating tissue presence. When using WAC compounding with RGC **c**, however, dropout data is held separate on the basis of scan-line incidence angle, and contributions from strong reflections persist

In Fig. 11a we see that the addition of RLW to WAC compounding boosts the peak-potential *match* score, while RGC increases scores over a broad range of threshold values. Figure 11b, on the other hand, reveals that the RGC is primarily responsible for increasing the accuracy of OLC compounding, while RLW provides an incremental boost.

With both WAC and OLC compounding, RGC and RLW improve reconstruction accuracies by $\approx 30\%$, with the highest achievable *match* score peaking at ≈ 0.65 . This relatively low score is attributed to a significant portion of the volume not being imaged because of dropout. We can see the effects of dropout by visually comparing the gold-standard volume with any of the other volumes in Fig. 10. In the following section, we show that the effects of dropout can be resolved by re-imaging “dropped-out” regions from different catheter configurations, in particular when RGC is employed.

Roof imaging

The left atrium roof is imaged from two catheter configurations, shown in Fig. 12a. The first (left) configuration yields poor reflection data because the ultrasound scan-lines inter-

sect the tissue’s surface at an angle nearly perpendicular to the surface normal. As a result, acquired ICE images from the first configuration suffer from significant dropout. The second (right) configuration, on the other hand, is well-suited for roof-imaging, with scan-lines intersecting the tissue’s surface at an angle nearly parallel to the surface normal. Depending upon whether RGC is employed to compensate for this dropout, the accuracy of volume-reconstruction varies dramatically.

In Fig. 12b we see a volume reconstructed using WAC compounding alone, and in Fig. 12c we see a volume reconstructed using WAC compounding with RGC. WAC compounding alone cannot distinguish between image data collected from the first and second configurations; all voxel contributions are given equal weight, and contributions from dropout data suppress those indicating tissue presence. As a result, an entire portion of the left atrium roof appears to be non-existent. When RGC is employed, however, contributions are naturally sorted on the basis of scan-line incidence angle. Dropout data do not contradict data indicating tissue presence unless the data were acquired from the same catheter configuration. The resulting reconstruction captures tissue surfaces more accurately.

Complete volume imaging

When we combine the data acquired from imaging the posterior wall, PV openings, and atrium roof, we see that RGC is critical for mitigating the effects of dropout in the final volume reconstruction, and RLW effectively filters out spurious reflections. Figure 13 shows a series of 3D-ICE volumes reconstructed using different compounding algorithms, compared against a gold-standard voxel map (Fig. 13a). The volumes are reconstructed using WAC alone (Fig. 13b), WAC with RGC (Fig. 13c), WAC with RLW (Fig. 13d), WAC with RGC and RLW (Fig. 13e), and OLC with RGC and RLW (Fig. 13f).

Without RGC (Fig. 13b, d), a significant portion of the roof’s surface is totally suppressed (as a result of the dropout data collected in Section “Roof Imaging”), but when RGC is applied (Fig. 13c, e and f), we are able to reconstruct the roof in its entirety. The addition of RLW (Fig. 13d, e and f) cleans up the reconstructed volume by eliminating contributions from ghost signals; the resulting 3D-ICE volumes are more visually useful for catheter guidance.

In Fig. 14 we see the *match* scores for WAC-compounded and OLC-compounded volumes over a range of classifier threshold values. Both RGC and RLW increase reconstruction accuracy for WAC-compounded volumes, with RLW responsible for achieving the highest overall *match* score, and RGC responsible for increasing scores over a wide range of threshold values (Fig. 14a). Using WAC alone, the peak

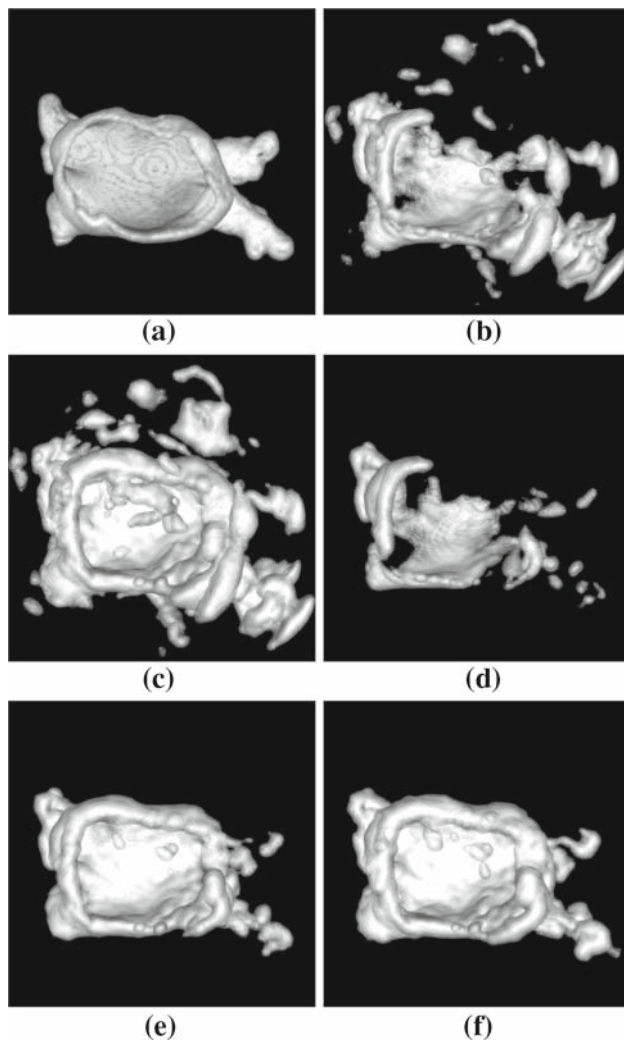


Fig. 13 Complete volume reconstruction. We reconstruct 3D-ICE volumes using ICE images acquired from all the catheter configurations shown in Fig. 8 and 12a. The volume in **a** is the gold-standard voxel map. The volume in **b** is reconstructed using WAC compounding alone. The volume in **c** is reconstructed using WAC with RGC, and the volume in **d** is reconstructed using WAC with RLW. Finally, the volume in **e** is reconstructed using WAC with RGC and RLW, and the volume in **f** is reconstructed using OLC with RGC and RLW

reconstruction accuracy is 0.475; after RGC and RLW are incorporated this value jumps to 0.862.

OLC reconstruction accuracies similarly increase with the addition of RGC and RLW (Fig. 14b). RGC is responsible for increasing OLC *match* scores more than two-fold; the magnitude of this improvement is related to the fact that our data set includes images suffering from dropout, which RGC is well-equipped to handle. Using OLC alone, the peak reconstruction accuracy is 0.245. After RGC is incorporated, peak accuracy jumps to 0.695, and with the addition of RLW, accuracy increases further to 0.962.

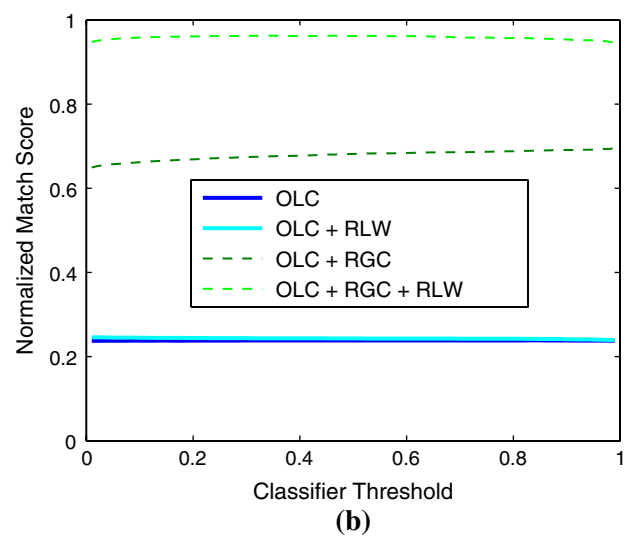
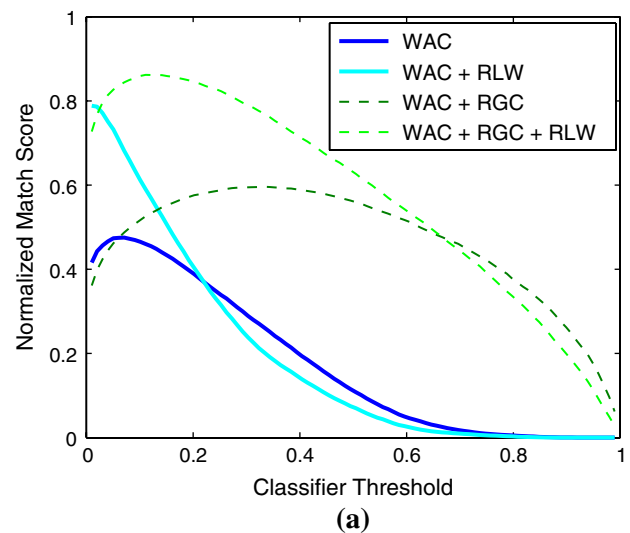


Fig. 14 Complete volume match scores. We combine data acquired from imaging the posterior wall, right and left PV openings, and the roof of the atrium to compute the overall *match* scores of our reconstructed volumes after thresholding. The gold-standard voxel map is used as the comparator. In **a** we see *match* scores for volumes reconstructed using WAC and in **b** we see *match* scores for volumes reconstructed using OLC

As before, OLC *match* scores hold steady across the entire range of threshold cutoffs, while WAC *match* scores are heavily tied to the particular cutoff value. For the volume reconstructed using WAC, RGC and RLW (Fig. 13e), the optimal threshold is 0.125, but in the absence of RLW (Fig. 13c), the optimal threshold is 0.32. As a result, visual presentation of reconstructed WAC data cannot be completely automated—to achieve the best overall volume rendering or surface reconstruction, the optimal classifier value should be known, and we cannot compute this value analytically. With OLC reconstructed volumes, however, we do not run into this problem.

Discussion

We have presented a novel approach to acquiring and reconstructing 3D-US volumetric data of the left atrium. We stitch together 2D-ICE images acquired from a multitude of configurations, and employ a combination of probabilistic techniques to reason about the likelihood of tissue presence given redundant information. By combining OLC with RGC and RLW, we are able to reconstruct highly accurate 3D-ICE volumes of a left atrium phantom, greatly exceeding what is measured when using a standard weighted-average approach.

As this study is a preliminary investigation, we have not evaluated anatomic motion compensation. Specifically, the positioning of the left atrial anatomy may drift cyclically along with patient breathing, and a 3D-US reconstruction algorithm not taking this into account may suffer from motion artifact. Solutions for respiration compensation include measuring patient-breathing, having the patient hold their breath briefly during imaging, or developing smarter reconstruction algorithms. In the future we hope to achieve the latter, relying on probabilistic theory built over the OGM framework discussed in Section “Occupancy-Likelihood Compounding”. In particular, we will incorporate the theory taken from *simultaneous localization and mapping* (SLAM), a field in robotics concerned with building “maps” of environments under uncertainty [29]. Applied to the catheter ablation setting, the “map” is our 3D-US reconstruction, the environment is the left atrium, and the uncertainty is related to anatomic movement that cannot be easily measured.

Our efforts are unique in the world of 3D-US literature as we are primarily concerned with voxel classification, related to a future desire to work on 3D-US segmentation. Our implementation of OLC automatically classifies voxels as being “occupied” or “clear,” precluding the need for an additional thresholding step for classification.

We have also folded in a response-grid compounding strategy that separates ultrasound contributions to the same voxel on the basis of scan-line incidence angle. RGC was shown to make our overall volume reconstruction more robust to dropout in images acquired from poorly chosen catheter configurations. The advantage of using RGC for real-time 3D-US reconstruction is that we need not be concerned with incorporating dropout data: as long as we find at least one probe configuration from which tissue reflections are strong, the reconstructed volume will correctly indicate tissue presence. This means we can continuously acquire new image data without having to stop each time we encounter signal dropout.

Finally, we have incorporated the results of a previous study which provided a method for iteratively registering ICE ultrasound to a CT-based anatomic surface mesh. By first registering the ICE catheter to the surface mesh, then proceeding with volume reconstruction, we can estimate where

we should expect to see ultrasound reflections and where we should not. This allows us to weight 2D-ICE data using RLW, effectively helping to filter out ghost-signals that are often observed when imaging inside the left atrium. RLW can potentially be used to filter out anatomic structures that are not part of the left atrium but still appear in the acquired 2D-ICE images, as well as reflections from other catheters that might be inside the left atrium during the procedure.

References

1. Manzke R, Zagorchev L, d’Avila A, Thiagalingam A, Reddy VY, Chan RC (2007) Rotational X-ray angiography: a method for intra-operative volume imaging of the left-atrium and pulmonary veins for atrial fibrillation ablation guidance. In: Proc. SPIE: medical imaging 2007: visualization and image-guided procedures, vol 6509, San Diego, pp 65,090T-1–65,090T-9
2. Thiagalingam A, Manzke R, d’Avila A, Ho I, Locke AH, Ruskin JN, Chan RC, Reddy VY (2008) Intraprocedural volume imaging of the left atrium and pulmonary veins with rotational X-ray angiography: Implications for catheter ablation of atrial fibrillation. *J Cardiovasc Electrophysiol* 19(3):293–300
3. Manzke R, Reddy V, Dalal S, Hanekamp A, Rasche V, Chan R (2006) Intra-operative volume imaging of the left atrium and pulmonary veins with rotational X-ray angiography. In: Medical image computing and computer-assisted intervention, Copenhagen, pp 604–611
4. Cannon J, Stoll J, Salgo I, Knowles H, Howe R, Dupont P, Marx G, del Nido P (2003) Real time 3-dimensional ultrasound for guiding surgical tasks. *Comput Aided Surg* 8(2):82–90
5. Linguraru MG, Vasilyev NV, Del Nido PJ, Howe RD (2007) Statistical segmentation of surgical instruments in 3-d ultrasound images. *Ultrasound Med Biol* 33(9):1428–1437
6. Novotny P, Stoll J, Dupont P, Howe R (2007) Real-time visual servoing of a robot using three-dimensional ultrasound. In: IEEE international conference on robotics and automation, Rome, pp 2655–2660
7. Zhang WY, Rohling RN, Pai DK (2004) Surface extraction with a three-dimensional freehand ultrasound system. *Ultrasound Med Biol* 30(11):1461–1473
8. Lee W, Idriss S, Wolf P, Smith S (2004) A miniaturized catheter 2-d array for real-time, 3-d intracardiac echocardiography. *Ultrasonics, ferroelectrics and frequency control*. *IEEE Trans Ultrason Ferroelectr Freq Control* 51(10):1334–1346
9. Poon TC, Rohling RN (2006) Three-dimensional extended field-of-view ultrasound. *Ultrasound Med Biol* 32(3):357–369
10. Knackstedt C, Franke A, Mischke K, Zarse M, Gramley F, Schimpf T, Plisiene J, Muehlenbruch G, Spuentrup E, Ernst S, Willems S, Kirchhof P, Schauerte P (2006) Semi-automated 3-dimensional intracardiac echocardiography: development and initial clinical experience of a new system to guide ablation procedures. *Heart Rhythm* 3(12):1453–1459
11. Solberg OV, Lindseth F, Torp H, Blake RE, Nagelhus Hernes TA (2007) Freehand 3d ultrasound reconstruction algorithms—a review. *Ultrasound Med Biol* 33(7):991–1009
12. Nelson T, Elvins T (1993) Visualization of 3d ultrasound data. *Comput Graphics Appl IEEE* 13(6):50–57
13. Sakas G, Schreyer LA, Grimm M (1995) Preprocessing and volume rendering of 3d ultrasonic data. *Comput Graphics Appl IEEE* 15(4):47–54

14. Elfes A (1989) Occupancy grids: A probabilistic framework for robot perception and navigation. Ph.D. thesis, Department of Computer and Electrical Engineering, Carnegie Mellon University
15. Thrun S (2003) Robotic mapping: a survey. In: Exploring artificial intelligence in the new millennium. Morgan Kaufmann Publishers Inc, San Francisco, pp 1–35
16. Koolwal AB, Barbagli F, Carlson CR, Liang DH (2008) An incremental method for registering electroanatomic mapping data to surface mesh models of the left atrium. In: Medical image computing and computer-assisted intervention—MICCAI 2008, vol 5242. Springer, Heidelberg, pp 847–854
17. O'Neill MD, Jaïs P, Hocini M, Sacher F, Klein GJ, Clémenty J, Haïssaguerre M (2007) Catheter ablation for atrial fibrillation. *Circulation* 116(13):1515–1523
18. Lickfett L, Dickfeld T, Kato R, Tandri H, Vasamreddy CR, Berger R, Bluemke D, Lüderitz B, Halperin H, Calkins H (2005) Changes of pulmonary vein orifice size and location throughout the cardiac cycle: dynamic analysis using magnetic resonance cine imaging. *J Cardiovasc Electrophysiol* 16(6):582–588
19. Okumura Y, Henz BD, Johnson SB, Bunch TJ, O'Brien CJ, Hodge DO, Altman A, Govari A, Packer DL (2008) Three-dimensional ultrasound for image-guided mapping and intervention: methods, quantitative validation, and clinical feasibility of a novel multimodality image mapping system. *Circ Arrhythmia Electrophysiol* 1(2):110–119
20. Singh SM, Heist EK, Donaldson DM, Collins RM, Chevalier J, Mela T, Ruskin JN, Mansour MC (2008) Image integration using intracardiac ultrasound to guide catheter ablation of atrial fibrillation. *Heart Rhythm* 5(11):1548–1555
21. Fenster A, Downey D (1996) 3-d ultrasound imaging: a review. *Eng Med Biol Mag IEEE* 15(6): 41–51
22. Forsberg F (2004) Ultrasonic biomedical technology; marketing versus clinical reality. *Ultrasonics* 42(1–9):17–27
23. Kim SH, Choi BI, Kim KW, Lee KH, Han JK (2003) Extended field-of-view sonography: advantages in abdominal applications. *J Ultrasound Med* 22(4): 385–394
24. Mercier L, Langø T, Lindseth F, Collins DL (2005) A review of calibration techniques for freehand 3-d ultrasound systems. *Ultrasound Med Biol* 31(4):449–471
25. Bushberg JT, Seibert JA, Edwin M, Leidholdt M, Boone JM (2002) The essential physics of medical imaging, 2nd edn. Lippincott Williams & Wilkins, Baltimore
26. Rohling R, Gee A, Berman L (1997) Three-dimensional spatial compounding of ultrasound images. *Med Image Anal* 1(3): 177–193
27. Howard A, Kitchen L (1996) Generating sonar maps in highly specular environments. In: Proceedings of the fourth international conference on control automation robotics and vision, pp 1870–1874
28. Martin MC, Moravec HP (1996) Robot evidence grids. Tech Rep CMU-RI-TR-96-06. The Robotics Institute, Carnegie Mellon University
29. Smith R, Self M, Cheeseman P (1990) Estimating uncertain spatial relationships in robotics. In: Autonomous robot vehicles. Springer, New York, Inc, pp 167–193